Mon. Not. R. Astron. Soc. **385,** 695–707 (2008) doi:10.1111/j.1365-2966.2008.12902.x

Combined analysis of weak lensing and X-ray blind surveys⋆

Joel Bergé,[1]† Florian Pacaud,[1,2] Alexandre Réfrégier,[1] Richard Massey,[3] Marguerite Pierre,[1] Adam Amara,[1] Mark Birkinshaw,[4] Stéphane Paulin-Henriksson,[1] Graham P. Smith[3,5] and Jon Willis[6]

[1]*Laboratoire AIM, CEA/DSM – CNRS – Université Paris Diderot, DAPNIA/SAp, 91191 Gif-sur-Yvette, France*
[2]*Argelander Institute für Astronomy, Universität Bonn, Auf dem Hügel 71, 53121 Bonn, Germany*
[3]*California Institute of Technology, 1200 E. California Blvd, Pasadena, CA 91125, USA*
[4]*Department of Physics, University of Bristol, Tyndall Avenue, Bristol BS8 ITL*
[5]*School of Physics and Astronomy, University of Birmingham, Edgbaston, Birmingham B15 2TT*
[6]*Department of Physics and Astronomy, University of Victoria, Elliot Building, 380 Finnerty Road, Victoria, BC, Canada V8V 1A1*

Accepted 2007 December 19. Received 2007 December 19; in original form 2007 August 29

ABSTRACT

We present a joint weak lensing and X-ray analysis of 4 deg^2 from the CFHTLS and *XMM*-LSS surveys. Our weak lensing analysis is the first analysis of a real survey using shapelets, a new generation weak lensing analysis method. We create projected mass maps of the images, and extract six weak-lensing-detected clusters of galaxies. We show that their counts can be used to constrain the power-spectrum normalization $\sigma_8 = 0.92^{+0.26}_{-0.30}$ for $\Omega_{\rm m} = 0.24$. We show that despite the large scatter generally observed in the mass–temperature (M–T) relation derived from lensing masses, tight constraints on both its slope and normalization M_* can be obtained with a moderate number of sources provided that the covered mass range is large enough. Adding clusters given by Bardeau et al. to our sample, we measure $M_* = 2.71^{+0.79}_{-0.61} \times 10^{14}\, h^{-1}\, {\rm M}_\odot$. Although they are dominated by shot noise and sample variance, our measurements are consistent with currently favoured values, and set the stage for future surveys. We thus investigate the dependence of those estimates on survey size, depth and integration time, for joint weak lensing and X-ray surveys. We show that deep surveys should be dedicated to the study of the physics of clusters and groups of galaxies. For a given exposure time, wide surveys provide a larger number of detected clusters and are therefore preferred for the measurement of cosmological parameters, such as σ_8 and M_*. We show that a wide survey of a few hundred square degrees is needed to improve upon current measurements of these parameters. More ambitious surveys covering 7000 deg^2 will provide the 1 per cent accuracy in the estimation of the power-spectrum and the M–T relation normalizations.

Key words: gravitational lensing – surveys – cosmological parameters – dark matter – large-scale structure of Universe – X-rays: galaxies: clusters.

1 INTRODUCTION

In the currently favoured hierarchical model of structure formation, clusters of galaxies have formed from the collapse of gravitational potential wells (e.g. Peebles 1980; Lacey & Cole 1993; Padmanabhan 1993; Lokas 2001) and are powerful cosmological probes. For instance, since they are sensitive to the expansion history of the Universe, their abundance and spatial distribution (e.g. Viana & Liddle 1996; Wang & Steinhardt 1998; Horellou & Berge 2005; Manera & Mota 2006; Nunes, da Silva & Aghanim 2006) and their mass function (e.g. Lokas, Bode & Hoffman 2004) depend on cosmological parameters, such as the dark energy equation of state parameter w (e.g. Basilakos 2003; Maor & Lahav 2005; Basilakos & Voglis 2007), or the power-spectrum normalization σ_8 (e.g. Seljak 2002; Pierpaoli et al. 2003). Several observational methods now permit the use of clusters of galaxies as cosmological probes, such as X-ray observations, weak gravitational lensing and the Sunyaev–Zeldovich effect.

⋆Based on observations obtained with MegaPrime/MegaCam, a joint project of Canada–France–Hawaii Telescope (CFHT) and CEA/DAPNIA, at the CFHT which is operated by the National Research Council (NRC) of Canada, the Institut National des Sciences de l'Univers of the Centre National de la Recherche Scientifique (CNRS) of France and the University of Hawaii. This work is based in part on data products produced at TERAPIX and the Canadian Astronomy Data Centre as part of the Canada–France–Hawaii Telescope Legacy Survey, a collaborative project of NRC and CNRS. It makes use of photometric redshifts produced jointly by TERAPIX and VVDS teams.

†E-mail: joel.berge@jpl.nasa.gov

Due to improvements in telescopes and techniques, X-ray studies are able to constrain cluster physics and the mass scaling relation with ever greater precision. For instance, the self-similarity for clusters of galaxies (Eke, Navarro & Frenk 1998; Arnaud, Aghanim & Neumann 2002) has been observationally verified. Nevertheless, adiabatic simulations still predicts a mass–temperature (M–T) relation with double the observed normalization (e.g. Nevalainen, Markevitch & Forman 2000; Finoguenov, Reiprich & Böhringer 2001) and the self-similarity assumption could break down at low temperatures ($T \leqslant 3$ keV). Thus, a steepening of the M–T relation is expected if galaxy groups underwent a preheating by supernovae, or a surge of entropy, in their early days (Bialek, Evrard & Mohr 2001; Muanwong et al. 2002). Recent evidence for this steepening was found by e.g. Nevalainen et al. (2000), Finoguenov, Reiprich & Böhringer (2001) or Arnaud, Pointecouteau & Pratt (2005) (APP05 hereafter), but could not be seen by e.g. Ettori, De Grandi & Molendi (2002), Castillo-Morales & Schindler (2003) and Vikhlinin et al. (2006). Moreover, the M–T normalization estimation is currently limited by systematics in measuring cluster masses from their X-ray profiles. This limitation can be lifted by using probes which are independent of the physical state of the cluster.

Beyond galaxy cluster physics, the M–T relation is needed by X-ray experiments to estimate the power-spectrum normalization σ_8. Measuring this parameter has triggered much effort in several observational areas. For instance, cosmic microwave background (CMB) experiments (e.g. Spergel et al. 2007) tend to a low value for $\sigma_8 (\leqslant 0.8)$, weak lensing experiments tend to higher values ($\geqslant 0.8$), and X-ray observations provide intermediate values.

Gravitational lensing does not depend on the underlying physics of clusters of galaxies or dark matter, but only on their potential wells, and on the Universe's geometry. Strong gravitational lensing has been used for galaxy clusters physics (e.g. Mellier, Fort & Kneib 1993; Kneib et al. 1995, 1996; Smail et al. 1997; Luppino et al. 1999; Smith et al. 2005) and measurement of σ_8 (e.g. Smith et al. 2003). Weak gravitational lensing is more difficult to measure (for reviews, see e.g. Mellier 1999; Bartelmann & Schneider 2001; Refregier 2003a; Munshi et al. 2006), and has taken longer to be detected (Bacon, Refregier & Ellis 2000; van Waerbeke et al. 2000; Wittman et al. 2000; Rhodes, Refregier & Groth 2001). Since then, particular attention has been given to cosmic shear, i.e. statistical cosmological weak lensing (e.g. Bacon et al. 2003; Heymans et al. 2005; Massey et al. 2005, 2007a; Hoekstra et al. 2006; Schrabback et al. 2007; Semboloni et al. 2006), in attempts to measure w and σ_8. It has also begun to be used as a tracer of the cosmic web (e.g. Massey et al. 2007b), and a way to detect and catalogue mass overdensities (e.g. Wittman et al. 2006; Gavazzi & Soucail 2007, GS07 hereafter, and Miyazaki et al. 2007). Beside the constraints it can bring to cosmology, it can be used as a complement to X-ray analyses of clusters of galaxies. Thanks to the physics-independent estimation of cluster masses, it appears as a unique method to calibrate the M–T relation for clusters of galaxies (e.g. Hjorth, Oukbir & van Kampen 1998; Huterer & White 2002; Pedersen & Dahle 2006; Bardeau et al. 2007). It has been shown that the uncertainty in the normalization of the M–T relation is the largest source of error in σ_8 measurements inferred from X-ray cluster analyses (Seljak 2002; Pierpaoli et al. 2003). An accurate M–T relation, obtained from combined weak lensing and X-ray analyses, will thus provide new insights not only on the σ_8 discrepancy, but also on galaxy cluster physics.

In this paper, we present the first joint analysis of weak gravitational lensing and X-ray wide-area surveys of a randomly selected patch of sky. The weak lensing survey is derived from the CFHTLS, and the X-ray survey from the *XMM*-LSS. The weak lensing analysis uses shapelets (Refregier 2003b; Refregier & Bacon 2003; Massey & Refregier 2005), a new generation shear measurement technique, which has been shown to achieve a few per cent accuracy in shear measurement from ground-based telescopes (Massey et al. 2007c). We analyse 1 deg^2 of the CFHTLS deep survey (the D1 field) and four contiguous square degrees of the CFHTLS Wide Survey, which enclose the D1 field. We create convergence maps for this region of the sky and give a catalogue of detections. We show how counting weak-lensing-selected clusters can provide an estimate of the power-spectrum normalization σ_8. We then show how the combination of weak lensing and X-ray analyses of clusters provides an estimate of the M–T relation normalization T_*, independent of clusters physical state. Finally, we investigate the impact of a joint weak lensing and X-ray survey strategy on the accuracy of the σ_8 and T_* measurement. We consider deep and wide weak lensing surveys, with the CFHTLS characteristics, combined with a blind X-ray survey of the same region of the sky.

The organization of the paper is as follows. Section 2 presents the surveys used in this paper, namely the CFHTLS and the *XMM*-LSS. The methods that we use are described in Section 3. We show how we estimate the weak lensing effect using shapelets, and how we generate convergence maps and detect clusters. We also briefly describe how the X-ray properties of clusters are obtained. Section 4 presents the convergence map we inferred from our weak lensing analysis, and gives a catalogue of the galaxy clusters that we detect. We then give our estimates of the normalization of the power spectrum and the M–T relation. We then show in Section 5 that combined blind surveys are necessary to get the best insights about those normalizations. The impact of survey strategy on those parameters estimations is discussed in Section 6. We conclude in Section 7.

2 DATA

2.1 Weak lensing: CFHTLS

The 'Canada–France–Hawaii Telescope Legacy Survey'[1] (CFHTLS), a joint France–Canada project, consists of three different surveys, namely the very wide survey, the Wide Synoptic Survey (referred to as 'wide survey' hereafter), and the deep survey. Once complete, the wide survey will cover 170 deg^2 (divided into four distinct patches ranging from 49 deg^2 to 72 deg^2) in five filters (u^*, g', r', i', z'), down to a magnitude $i' \approx 24.5$. Its main goal is the study of large-scale structures by weak gravitational lensing and galaxy counts. The deep survey covers four different fields, each with an area of 1 deg^2, in the same five filters, down to $i' \approx 28.5$. It is primarily intended for Type Ia supernovae studies but it is also useful for measuring large-scale structures. The CFHTLS images were obtained from observations with the MegaCam camera, made of a 36 CCD mosaic, of 2048 $\times$ 4196 pixel each, with a 1 deg^2 field of view (Boulade et al. 2003).

In this paper, we present the weak gravitational lensing based mapping of 4 deg^2 of the wide survey (W1 patch), which include the 1 deg^2 field of the deep survey (D1 field), using both W1 and D1 images. The geometry of the fields that we use is shown in Fig. 1. The data processing (astrometry, photometric calibration, stacking of images) has been done by the CFHT community and Terapix.[2] We use W1 images optimized for weak lensing: each field is the combination of seven stacked images, each of 620-s exposure time.

[1] http://www.cfht.hawaii.edu/Science/CFHLS/.
[2] http://terapix.iap.fr.

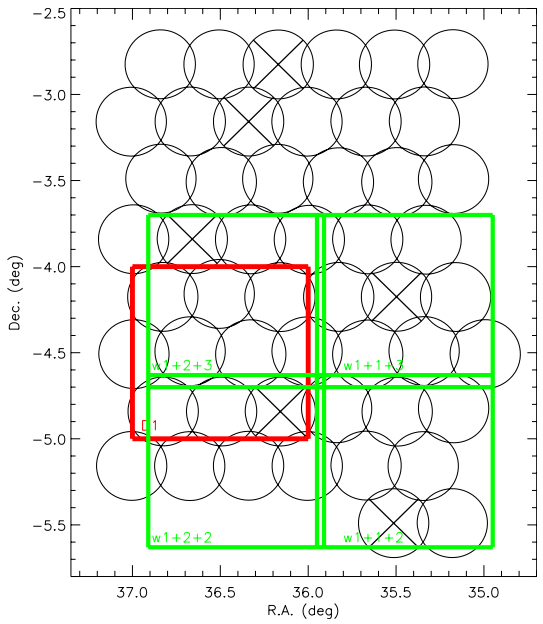

Figure 1. Layout of the surveys. The red square is the CFHTLS D1 field. The four green squares are the four CFHTLS W1 fields used in this paper. Circles represent the *XMM*-LSS pointings available in that region, prior to *XMM* AO5 (Pacaud et al. 2007). Here, we only used those lying within the optical data. Those marked by a cross are strongly affected by flares and are being re-observed (see the electronic version of the journal for a colour version of this figure).

We use the T0003 release of the D1 field, consisting of 275 stacked images, with a total 37.4-h exposure time. The average seeing is 0.7 arcsec. We masked parts of the images with saturated stars and/or too high a noise, by hand, so as not to bias our weak lensing results. This operation removes 10 per cent of the original area covered by the data. We do not mask the ghosts created by spurious reflections on the telescope optics around saturated stars, but we eventually remove the galaxies that they cover from our catalogues, since they are too noisy. The average galaxy density is 28 arcmin^{-2} in the D1 image, and 13 arcmin^{-2} in the W1 images.

2.2 X-ray: *XMM*-LSS

Designed to cover an area of several tens of square degrees up to a redshift $z = 1$, the *XMM*-LSS survey aims at detecting a significant fraction of clusters of galaxies, in order to constitute a sample suited to cosmological studies (Pierre et al. 2004). Its nominal exposure times are 10 ks, and have been raised up to 20 ks for the *XMM* Medium Deep Survey (Chiappetti et al. 2005), a 2-deg^2 region included in the *XMM*-LSS, which covers the CFHTLS D1 field. In this paper, we use 4 deg^2 of the *XMM*-LSS which cover our 4-deg^2 CFHTLS data. The *XMM* pointings are shown in Fig. 1. The raw X-ray observations reduction is presented in Pacaud et al. (2006).

3 METHOD

3.1 Weak lensing cluster detection

Introduced in Refregier (2003b), Refregier & Bacon (2003) and Massey & Refregier (2005), shapelets are a complete, orthogonal set of basis functions with which one can analytically decompose galaxy shapes. They can be seen as fundamental shapes: a particular galaxy can be represented by a particular sum of shapelets basis functions $\chi_{n,m}$, weighted by coefficients $f_{n,m}$. Their rich formalism provides an intuitive and analytic form for geometrical transformations (such as smear, shear, rotation) and for (de)convolution. Hence, they allow one to analytically describe the smearing of the point spread function (PSF) and the shear of galaxies, properly correcting for the PSF. The shear estimation they provide has been shown to reach the needed accuracy for the CFHTLS specifications by the STEP project (Massey et al. 2007c).

Our full pipeline will be described in an upcoming paper (Bergé et al., in preparation). We briefly summarize it here. Each sufficiently bright and non-saturated star is first decomposed into shapelets. A polynomial interpolation of each shapelet coefficient then provides a model of its spatial variations across the image. We are thus able to reconstruct the shape of the PSF at the position of each galaxy, the condition necessary for deconvolving it from the galaxies' shapes. Several stringent tests then validate our PSF model. In particular, we require that the ellipticity distribution, and the two point correlation functions of the ellipticity, of the residuals between observed stars and their shapelet models are consistent with zero. We also require that the cross-correlation between stars and galaxies ellipticity, when corrected from the PSF, is consistent with zero. The shape of galaxies is finally measured by decomposing them into shapelets, while deconvolving from the PSF, as shown in Massey & Refregier (2005).

A shear estimator is created from the shapelet decompositions of galaxies, as prescribed by Massey et al. (2007d):

$$\gamma = \frac{f_{2,2}}{P^{\gamma}}, \tag{1}$$

where the shear susceptibility $P^{\gamma} = \langle f_{0,0} - f_{4,0} \rangle / \sqrt{2}$ is fitted on the magnitude-size plane for galaxies. The coefficients are complex numbers. The shear γ of equation (1) is the complex notation for shears, $\gamma = \gamma_1 + i\gamma_2$.

To increase the signal-to-noise ratio of our measurements, we give to each galaxy g a minimum variance weight $w_g = (\sigma^2_{\varepsilon,g} + \sigma^2_{P_{\gamma},g} + \sigma^2_{\rm int})^{-1}$, where $\sigma_{\varepsilon,g}$ is the error on shape measurement for galaxy g, $\sigma_{P_{\gamma},g}$ the error on the measurement of its shear susceptibility, and $\sigma_{\rm int}$ is the intrinsic ellipticity dispersion, set to $\sigma_{\rm int} = 0.3$. Slightly changing $\sigma_{\rm int}$ would be equivalent to giving more or less weight to our measurement errors, and would mostly affect the error bars in the shear measurement. The eventual peak detection would not be affected by such slight changes. This weighting scheme is equivalent to smoothly selecting the most useful galaxies for shear measurement. For instance, the faintest are down-weighted. It therefore provides us with effective densities of $n_{\rm eff} \approx 20$ and 9 useful galaxies per square arcminute, in the D1 and W1 images, respectively. Then, a direct inversion in Fourier space of the pixelized shear map allows us to infer a convergence (i.e. projected mass) map (Kaiser & Squires 1993) of the images. Structures in this mass map are extracted from the noise using a Gaussian filter. Figs 2 and 3 show the convergence maps that we inferred from our data. These are described in Section 4.1. While constructing a convergence map, we also create a signal-to-noise ratio map, the signal-to-noise ratio being defined as

$$\nu(x, y) = \frac{\kappa(x, y)}{\sigma_{\kappa}(x, y)}, \tag{2}$$

where κ (x, y) is the convergence at the (x, y) sky coordinates, and $\sigma_{\kappa}(x, y)$ its rms error. The rms error $\sigma_{\kappa}(x, y)$ is computed using Monte Carlo simulations in which the input galaxies are positioned like the observed ones but with randomized shape orientations.

Structures are then searched for in the filtered convergence map, and their astrometry provided, by the SEXTRACTOR software (Bertin

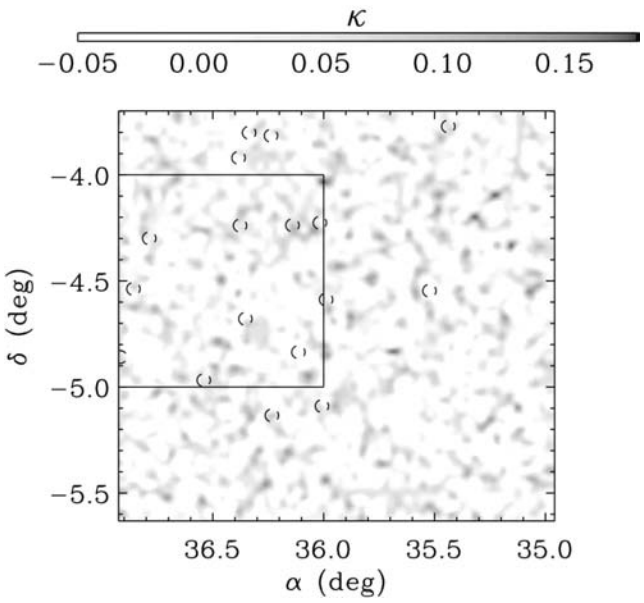

Figure 2. Convergence map inferred from our weak lensing measurement of the W1 field. The square in the W1 map shows the boundaries of the D1 field (Fig. 3). The map is smoothed by a 2.3 arcmin full width at half-maximum (FWHM) Gaussian. Dashed circles mark C1 X-ray clusters.

& Arnouts 1996). They are extracted according to their signal-to-noise ratio peak, read from the signal-to-noise ratio map. Hereafter, we define a 'significant structure' as a detection with a signal-to-noise ratio greater than 2.5. Their mass is related to their integrated convergence through the lensing geometry, and can be estimated when their redshift and the redshift distribution of background galaxies are known. To account for the latter, we use the normalized distribution

$$n(z) = \frac{\beta}{z_s \Gamma\left(\frac{1+\alpha}{\beta}\right)} \left(\frac{z}{z_s}\right)^{\alpha} \exp\left[-\left(\frac{z}{z_s}\right)^{\beta}\right], \quad (3)$$

where the parameters α, β, z_s are given for the wide images by Benjamin et al. (2007) $(\alpha, \beta, z_s) = (0.836, 3.425, 1.171)$. To account for $n(z)$ in the D1 image, we fit the photometric redshift distribution of Ilbert et al. (2006) in the CFHTLS D1 field, and obtain $(\alpha, \beta, z_s) = (0.828, 1.859, 1.148)$. van Waerbeke et al. (2006) have shown that errors in the $n(z)$ fit are subdominant compared to Poisson noise and sample variance for the measurement of cosmological parameters. We thus neglect them hereafter.

We measure a cluster's virial mass by averaging its convergence in an aperture large enough that we can assume that the entire cluster is captured. The aperture corresponds to the region enclosed in the 2σ level of the cluster's convergence map. This technique is similar to using a ζ-statistic (Fahlman et al. 1994), with infinitely large annulus around the cluster, provided that the convergence in the entire field averages to 0. We verified this latter point, thus validating our choice. Note that because of the small number density of background sources, we cannot reliably fit a shear profile around clusters (see e.g. Paulin-Henriksson et al. 2007, for an example of mass estimation using two profile fits around the galaxy cluster Abell 209). We then convert the virial mass into $M_{200,c}$, the mass enclosed in the sphere of mean overdensity 200 times higher than the critical density, using the recipe from Hu & Kravtsov (2003). Hereafter, we will note $M_{200,c}$ more briefly M_{200}.

Weak lensing is affected by the entire mass distribution along the line of sight. As a result, the weak lensing mass measurement of one cluster is biased by projection effects. It has been shown, using different mass estimators, that large-scale structures in the line of sight, and near the target cluster, introduce errors ranging from a few per cent (Reblinsky & Bartelmann 1999; Hoekstra 2001, 2003; Clowe, De Lucia & King 2004) to a few tens of per cent (Metzler, White & Loken 2001; de Putter & White 2005). In this paper, we assume that they produce a 20 per cent error, added in quadrature to the shear measurement error.

3.2 X-ray cluster detection and analysis

The X-ray cluster detection pipeline has been described in Pacaud et al. (2006). It takes account of the Poisson nature of the X-ray images, to extract and analyse clusters of galaxies in a two-step procedure. Clusters are first detected by a multiresolution wavelet filter (Starck et al. 1998). Then, each source is analysed using a maximum likelihood profile fitting procedure, and its X-ray properties assessed. Three classes of extended sources have been defined (Pacaud et al. 2006; Pierre et al. 2006): (1) the C1 class contains the highest surface brightness sources, and is uncontaminated; (2) the C2 class allows for 50 per cent contamination, and contains less bright extended sources; (3) finally, the C3 class contains optically confirmed sources with apparent X-ray emission, which were not selected as C1 or C2. In this paper, we only consider C1 class detections, representative of the most massive objects seen in the *XMM*-LSS. The redshift of detected clusters has been measured using spectroscopic observations from a number of telescope and instrument combinations detailed in table 2 of Pierre et al. (2006). Their temperature estimation is described in Willis et al. (2005).

Pacaud et al. (2007) have extracted and analysed 29 C1 clusters from 5 deg^2 of the *XMM*-LSS data (shown in Fig. 1), which contain our 4 deg^2 optical data. Among other things, they have measured their luminosity and temperature. Here, we take into account their 16 clusters which are enclosed in the fields of our CFHTLS data, making use only of their temperature and redshift. They are listed in Table 1. Note that the cluster XLSSC053 is in the G12 *XMM*-LSS pointing (shown by the cross in the D1 field, in Fig. 1), which was not used when Pacaud et al. (2007) analysed the *XMM*-LSS observations. This pointing has been re-observed, and the X-ray characteristics of XLSSC053 are listed in Table 1.

4 RESULTS

In this section, we give the properties of clusters of galaxies detected with our weak lensing pipeline. Counting the weak lensing detections allows us to constrain the matter power-spectrum normalization σ_8. We then use the weak lensing mass of the detected groups to calibrate the M–T relation for clusters of galaxies.

4.1 Convergence maps and cluster catalogue

Fig. 2 shows the 4 deg^2 of the W1 field that we considered. No significant overdensity (i.e. with $\nu \geqslant 2.5$) has been detected. As we will quantitatively show in Section 4.2.1, this is consistent with the expected cluster counts for this survey. The black square in the image shows the position of the D1 field. Since there are around 20 galaxies arcmin^{-2}, we expect more significant detections in this deep field (see Section 4.2.1). The upper panel of Fig. 3 shows the convergence map that we obtained from our weak lensing analysis of the D1 field. Due to the varying level of noise in our map, which varies independently of κ, two peaks with the same κ value do not necessarily have the same significance. That results in the rejection of seemingly significant structures, such as the peak around $(\alpha, \delta) =$

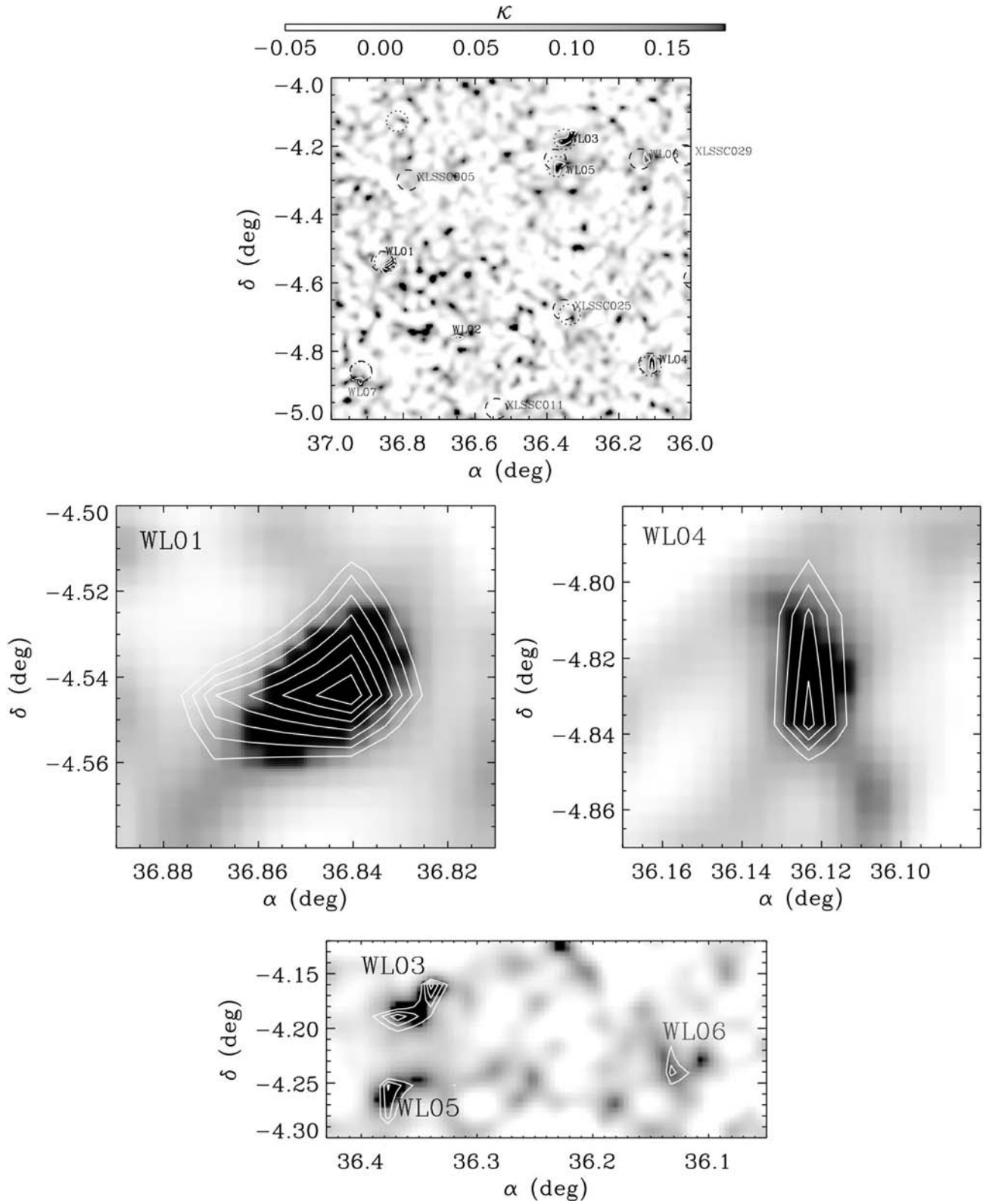

Figure 3. Convergence map inferred from our weak lensing measurement of the D1 field. The convergence κ is shown for the entire field on the upper panel. Lower panels show zooms on cluster candidates WL01, WL04, and the region surrounding WL03, WL05 and WL06. In the upper panel, contours levels start at 2.2σ, with an increment of 0.5σ. In the lower panels, they start at 2.2σ, with an increment of 0.2σ. The maps are smoothed by a 1.1 arcmin FWHM Gaussian. In the upper panel, dashed circles mark X-ray clusters, and dotted circles show GS07's KSB weak lensing detections. Clusters detected by our shapelets weak lensing measurement are labelled WL*id*, and X-ray clusters not detected by weak lensing are labelled by their *XMM* name. All clusters are listed in Table 1. For clarity, false detections near edges are not shown.

Table 1. Clusters catalogue. Besides the clusters that we detect through our shapelet weak lensing measurement, we also list clusters seen by GS07, and selected as C1 clusters in the *XMM*-LSS. Weak lensing detections' significance is given for D1 and W1, even if no detection appears in W1. M_{200}(WL) is the cluster weak lensing mass. M_{200}(X) is the mass estimated from X-ray profile, extrapolated from R_{500} to R_{200}, with respect to M_{500} masses given by Pacaud et al. (2007), and must be used with caution (see text).

Weak lensing cluster ID	XLSSC number	GS07 ID	RA (°)	Dec. (°)	z	Significance D1/W1	M_{200}(WL) ($10^{13}\,h^{-1}\,M_\odot$)	T_X (keV)	M_{200}(X)[c] ($10^{13}\,h^{-1}\,M_\odot$)	Notes
WL01	013	Cl03	36.8497	−4.5481	0.31	3.61/–	$8.2^{+2.5}_{-1.9}$	$1.0^{+0.1}_{-0.1}$	2.1	
WL02	–	–	36.6589	−4.7516	–	3.09/–	–	–	–	
WL03	–	Cl04	36.3628	−4.1886	0.32[a]	2.91/–	$8.9^{+2.6}_{-2.2}$	–	–	
WL04	053	Cl02	36.1229	−4.8341	0.50[b]	2.90/–	$10.3^{+3.0}_{-2.6}$	$3.4^{+3.1}_{-1.0}$	5.0	*XMM*-LSS pointing Not observed in Pacaud et al. (2007)
WL05	041	Cl14	36.3723	−4.2604	0.14	2.62/–	$4.9^{+1.6}_{-1.2}$	$1.3^{+0.1}_{-0.1}$	3.5	
WL06	044	–	36.1389	−4.2384	0.26	2.48/–	$7.2^{+2.3}_{-1.7}$	$1.3^{+0.2}_{-0.1}$	3.7	Just below detection threshold in GS07's catalogue
WL07[d]	022	Cl07	36.9167	−4.8606	0.29	2.42/–	–	$1.7^{+0.1}_{-0.1}$	5.3	Near a mask
–	025	Cl05	36.3375	−4.6925	0.26	–/–	–	$2.0^{+0.2}_{-0.2}$	6.5	Under a mask
–	–	Cl10	36.8167	−4.1269	–	–/–	–	–		
–	029	–	36.0172	−4.2260	1.05	–/–	–	$4.1^{+0.9}_{-0.7}$	13.9	Too high redshift
–	011	–	36.5410	−4.9680	0.05	–/–	–	$0.64^{+0.06}_{-0.04}$	1.0	
–	005	–	36.7866	−4.2995	1.05	–/–	–	$3.7^{+1.5}_{-1.}$	16.5	Too high redshift
–	006[†ger]	–	35.4382	−3.7717	0.43	X/–	–	$4.8^{+0.6}_{-0.5}$	30.4	Near an edge
–	040[†ger]	–	35.5232	−4.5463	0.32	X/–	–	$1.6^{+1.1}_{-0.3}$	6.8	
–	049[†ger]	–	35.9892	−4.5880	0.49	X/–	–	$2.2^{+0.9}_{-0.5}$	5.0	
–	018[†ger]	–	36.0079	−5.0903	0.32	X/–	–	$2.0^{+0.7}_{-0.4}$	8.0	
–	021[†ger]	–	36.2338	−5.1340	0.08	X/–	–	$0.68^{+0.04}_{-0.02}$	1.8	
–	001[†ger]	–	36.2378	−3.8156	0.61	X/–	–	$3.2^{+0.4}_{-0.3}$	14.3	
–	008[†ger]	–	36.3367	−3.8014	0.30	X/–	–	$1.3^{+0.7}_{-0.2}$	2.1	
–	002[†ger]	–	36.3841	−3.9198	0.77	X/–	–	$2.8^{+0.8}_{-0.5}$	9.6	

[a]Tomographic redshift (GS07).[b]Photometric redshift (Aussel et al. in preparation).[c]Rough estimates based on the isothermal assumption and extrapolated from M_{500} given by Pacaud et al. (2007).[d]X-ray coordinates.[†ger]Outside D1.

(36.°75, −4.°75). Significant structures are marked out by the white contours, which start at 2.2σ, with an increment of 0.5σ. The lower panels show individual candidate clusters in more details. In these, contours start at 2.2σ, with an increment of 0.2σ. Even though we consider as significant a structure with $\nu \geqslant 2.5$, we plot the 2.2σ contours as a way to show the extension of our detections. Dashed circles mark X-ray clusters, and dotted circles mark the weak lensing detections of GS07. GS07 measured the shear in the D1 field using the KSB method (Kaiser, Squires & Broadhurst 1995).

Table 1 summarizes the measured characteristics of the clusters that we detect, together with all X-ray and GS07's detections in the region. The clusters that we detect through our shapelets weak lensing analysis are labelled with WL*id*, where *id* runs from 00 to 07, and are sorted by decreasing significance. Their labels are listed in the first column. Their official *XMM* names are given in column (2), and GS07's IDs in the third column. X-ray clusters marked by a † are outside the D1 field. Columns (4) and (5) give their position. Column (6) lists their spectroscopic redshifts, except for clusters WL03, for which a tomographic redshift is given, and WL04 for which a photometric redshift is given (Aussel et al. in preparation). The significances of the weak lensing detections are listed in column (7), in D1 and W1. A '–' means that the cluster is not detected; a 'X' means that the cluster is outside the D1 field. Columns (8) and (9) give their weak lensing mass M_{200}(WL) and X-ray temperature, respectively. Column (10) gives the mass estimate from the X-ray data, $M_{200}(X)$. As in Pacaud et al. (2007), these were evaluated under the assumption of an isothermal β-model gas distribution in hydrostatic equilibrium with the cluster's potential well. In this earlier work, the associated statistical errors were generally dominated by the temperature measurement uncertainty ($\delta M/M \approx \delta T/T$ of the order of 10–25 per cent). Here, the error on the emission profile can also become quite significant because we estimate the masses within R_{200} instead of R_{500} where the X-ray emission starts to vanish. Moreover, it was shown by Vikhlinin et al. (2006) and Rasia et al. (2006) that the isothermal β-model assumption leads to an underestimation of the total mass, by up to 40 per cent for low-mass systems. For these reasons, we decided not to provide error bars for our X-ray masses. Finally, column (11) gives some details about weak lensing detections, explaining for instance why we chose not to take them into account, or why we do not detect a cluster seen by another method. Among the rejection criteria are the proximity to an edge or to a masked region, the mass inversion procedure being sensitive to missing data and to edge effects. In that sense, and for clarity, the detections closest to edges have been removed from Figs 2 and 3.

Clusters WL01, WL04 and WL05 have unequivocal counterparts both in our X-ray catalogue and in GS07's KSB one. No significant C1 X-ray source has been selected around WL02, and it remains invisible to GS07. Moreover, a visual inspection of the optical images does not show any galaxy overdensity around it. No significant C1 X-ray source has been detected at the position of WL03, even though it is also seen by GS07. Cluster WL06 lies just below our detection threshold ($\nu = 2.48$). Nevertheless, since GS07 detect it (though just below the detection threshold they use for their analyses) and since it is also detected by our X-ray analysis, we decided to list it, and to assess its weak lensing characteristics. The significance of cluster WL07 is even lower ($\nu = 2.42$). Since it is found close to the XLSSC022 cluster (which coincides with GS07's Cl07), we show

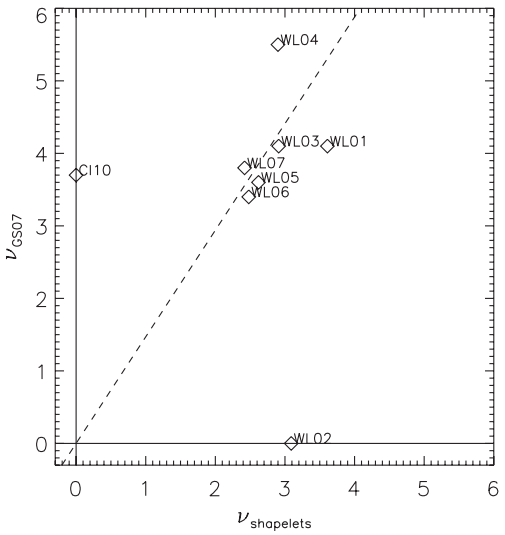

Figure 4. Comparison between our detection significance and those of GS07. Symbols are data points. Cl10 is detected by GS07, but remains invisible to our pipeline. The dashed line features the expected relation between clusters' significance in both analyses, $\nu_{GS07} = 1.47\nu_{shapelets}$.

its contours in Fig. 3 and list it in Table 1. However, it lies near an edge and a mask, so that its weak lensing characteristics are likely to be biased. We thus do not measure its mass, and will not take it into account in what follows. Cluster XLSSC025 (GS07's Cl05) is under a mask, and cannot be detected by our pipeline.

In summary, out of our seven shapelet weak lensing detections, four (WL01, WL04, WL05 and WL07) have a counterpart both in our X-ray catalogue and in the KSB weak lensing catalogue by GS07, even though we remove WL07 from our subsequent analyses. One detection (WL02) appears only in our catalogue. One (WL06) has an X-ray counterpart, and appears in GS07's map, but just below the detection threshold they use for their analysis. Finally, one (WL03) has a counterpart in GS07's catalogue, but is not selected as a C1 X-ray cluster. This proves a good agreement between the three cluster detection methods used in those observations. X-ray clusters XLSSC005 and XLSSC029 are at too high a redshift to be detected with our surveys. Cluster XLSSC011 is too close and not massive enough to be detected by weak lensing, as will be shown in Section 4.2.1.

Fig. 4 compares the significance of our detections with that given by GS07. We make use of WL06, even though GS07 did not use it, but gave its significance. Given our weak lensing measurement characteristics ($n_{\rm eff} = 19\,{\rm arcmin}^{-2}, \sigma_{\rm int} = 0.3$) and theirs ($n_{\rm eff} = 25.3\,{\rm arcmin}^{-2}, \sigma_{\rm int} = 0.23$), equation (4) below allows us to compute the expected proportionality factor between our detections' significance $\nu_{\rm shapelets}$ and theirs, $\nu_{\rm GS07}$. We expect $\nu_{\rm GS07} = 1.47\nu_{\rm shapelets}$. This relation is shown by the dashed line in Fig. 4. The significance of clusters in both catalogues scales as expected. One should note that this relation depends on the measurement characteristics for both methods in those particular experiments, and should not be used as a final comparison between KSB and shapelets. More comparison on real data will be needed in order to explore this issue.

While X-ray masses listed in column (10) of Table 1 must be taken with caution, they can be compared to the weak lensing masses listed in column (8). Although one can notice an order of magnitude agreement between M_{200}(WL) and M_{200}(X), masses estimated from X-ray data seem slightly underestimated. This is consistent with the previously mentioned bias arising from the isothermal β-model parametrization.

While they do not provide strong statistics, our detections can be used to estimate σ_8, as shown below. Four detections have an X-ray counterpart and can thus be used to constrain the M–T relation, provided that we add clusters from another catalogue. This is described below.

4.2 Cluster number counts

4.2.1 Weak lensing selection function

A weak gravitational lensing selection function can be computed analytically (see e.g. Hamana, Takada & Yoshida 2004; Marian & Bernstein 2006) from the signal-to-noise ratio of a halo in a given cosmology and weak lensing survey parameters. We derive such a selection function, using an optimal match filter, in Bergé, Amara & Réfrégier (in preparation). In an observation characterized by a number density of background galaxies n_g, an NFW halo of convergence κ has signal-to-noise ratio:

$$\nu = \frac{\sqrt{n_g}}{\sigma_\gamma}\sqrt{\int {\rm d}^2x\,\kappa^2(x)}, \tag{4}$$

where σ_γ is the rms shear error per galaxy, and where we neglect projection effects and sample variance, which have been shown to have subdominant effects (Marian & Bernstein 2006).

Our selection function is shown in Fig. 5 in the mass–redshift plane, for our deep ($n_g = 20\,{\rm arcmin}^{-2}, \sigma_\gamma = 0.3$, thick black) and our wide ($n_g = 9\,{\rm arcmin}^{-2}, \sigma_\gamma = 0.4$, red) surveys, in a cosmological model based on the three-year *Wilkinson Microwave Anisotropy Probe* results (*WMAP*3; Spergel et al. 2007), (h, $\Omega_{\rm m}h^2$, $\Omega_{\rm b}h^2$, σ_8, w) = (0.73, 0.127, 0.0223, 0.76, −1). We use the redshift distributions for background galaxies given by equation (3).

Fig. 5 shows, from bottom to top, the minimum detectable mass for a halo at 2, 3 and 4σ detection thresholds. The deep and wide selection functions have different slopes, as a consequence of their different redshift distribution for background galaxies. Symbols represent the position, in the redshift–mass plane, of clusters listed in Table 1. We use the weak lensing mass M_{200}(WL) for WL01, WL03, WL04, WL05 and WL06 (thick square symbols) and the X-ray mass M_{200}(X) for other clusters (diamonds). Although we detect cluster XLSSC022 (WL07), we do not assess its gravitational mass, and thus show its X-ray mass in Fig. 5. Cluster XLSSC025 should be detectable (and is detected by GS07), but it is under a mask in our analysis. Triangle symbols (labelled † in Table 1) correspond to C1 X-ray clusters in W1 that are outside the D1 region. It is clear from Fig. 5 that they can not be detected by our weak lensing analysis of W1. Only XLSSC006 should be seen, at the 2σ level. However, its detection is plagued by its proximity to the edge of the image.

Also shown in Fig. 5 are the X-ray selection functions, for 50 per cent and 80 per cent detection probabilities (dashed lines) as estimated by Pacaud et al. (2007).

Fig. 5 shows an excellent agreement between the clusters characteristics and their predicted detectability by weak gravitational lensing.

4.2.2 Number counts

From equation (4), the expected number of haloes detected above a certain significance can be computed using a Press–Schechter approach (Press & Schechter 1974). For this purpose, we use the

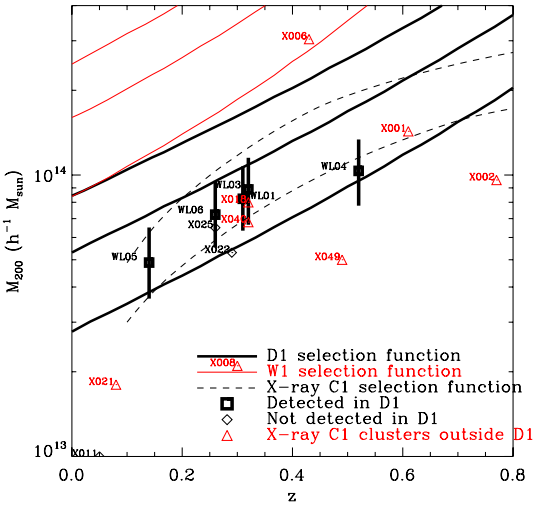

Figure 5. Weak lensing selection function for a survey like D1 (thick black; $\sigma_{\rm int} = 0.3, n_g = 20$ arcmin^{-1}, redshift distribution as equation 3) and W1 (red; $\sigma_{\rm int} = 0.4, n_g = 9$ arcmin^{-1}, redshift distribution as equation 3), assuming a *WMAP*3 cosmology in each case. From bottom to top, lines correspond to 2, 3 and 4σ significance. Dashed lines show the X-ray selection function, corresponding to 50 and 80 per cent detection probability (Pacaud et al. 2007, fig. 18, lower and upper curves, respectively). Thick square symbols are our detections in the D1 data, labelled by their ID; they are not detectable in the W1 data. Diamonds are clusters detected either by GS07 or by X-ray analysis, in D1, that we do not detect for reasons listed in the text. Red triangles are C1 X-ray clusters lying outside the D1 region. Except for the thick square symbols [for which we use the weak lensing mass M_{200}(WL)], we use the X-ray mass M_{200}(X). Except XLSSC006 (labelled for visibility as X006), they cannot be detected by a weak lensing experiment in the W1 data. XLSSC006 is not detected because of its proximity to an edge (see the electronic version of the journal for a colour version of this figure).

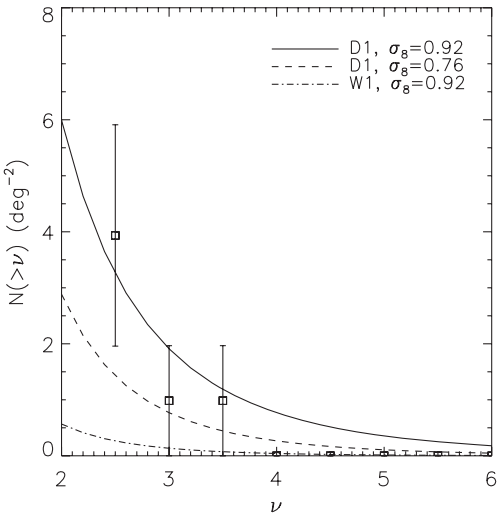

Figure 6. Cumulative cluster number density as a function of weak lensing detection significance, in the D1 data. The error bars include shot noise and sample variance. The dashed line shows the expected number counts in a *WMAP*3 cosmology, for the survey's characteristics. The solid line is our best fit, when varying σ_8 ($\sigma_8 = 0.92$). The dot–dashed line is the expected number counts for the wide survey, with $\sigma_8 = 0.92$.

Jenkins et al. (2001) mass function to estimate the number of haloes that we can detect, as a function of significance threshold. Curves in Fig. 6 show such counts for different σ_8 and survey depths. Miyazaki et al. (2002) already used this statistic to discriminate between halo profile models. It is used here to measure σ_8.

Most of our detections are validated by corresponding objects either in the catalogue of GS07 or our X-ray C1 cluster catalogue. Nevertheless, despite its relative high significance, WL02 does not have such independent support. We indeed consider it as a false detection, and do not take it into account for cluster counts. We then estimate the number of false detections from Monte Carlo simulations. For this purpose, we input galaxies at the position of the actual ones, but randomize their shear, and look for detections with significance higher than 2.5σ. The convergence maps that we infer from them show only false detections. We find that, in this particular experiment, we expect only one false detection above the 2.5σ level. This is thus consistent with removing WL02. For this counting purpose, we remove WL06 and WL07 from our catalogue, since they do not reach the 2.5σ level. The symbols in Fig. 6 represent our cumulative counts, corrected from false detections. Their error bars include the effects of shot noise and sample variance, computed from Hu & Kravtsov's (2003) analytic formula. We then fit the expected number counts to our data as a function of σ_8, keeping all other parameters constant. In order to avoid covariance between our data points in the cumulative counts depicted by Fig. 6, we performed the fit on the expected differential number counts $\mathrm{d}N/\mathrm{d}\nu$ (ν). We find $\sigma_8 = 0.92^{+0.26}_{-0.30}$ (at the 68.3 per cent confidence limit), for $\Omega_{\rm m} = 0.24$. Despite large error bars, we can set interesting constraints thanks to the strong dependence of these counts on σ_8, as shown by the difference between the solid and dashed curves in Fig. 6. The dashed line shows the expected cumulative number counts for the deep survey in a *WMAP*3-like universe ($\sigma_8 = 0.76$). The solid line is our best fit ($\sigma_8 = 0.92$). The dot–dashed line shows the expected number density on the wide survey, with $\sigma_8 = 0.92$.

4.3 Mass–temperature relation

Under the virial equilibrium assumption, the mass and temperature of a cluster are related by the following scaling relation (Pierpaoli et al. 2003)

$$\frac{M_{\rm vir}(T,z)}{10^{15}\,h^{-1}\,{\rm M}_\odot} = \left(\frac{T}{T_*}\right)^{3/2} \left[\Delta_{\rm c}(z)E(z)^2\right]^{-1/2} \left[1 - 2\frac{\Omega_\Lambda(z)}{\Delta_{\rm c}(z)}\right]^{-3/2}, \quad (5)$$

where $M_{\rm vir}$ is the virial mass, T is the virial temperature, T_* is a normalization factor and $E(z)^2 = \Omega_{\rm m}(1+z)^3 + \Omega_\Lambda + \Omega_{\rm k}(1+z)^2$. $\Delta_{\rm c}(z)$ is the overdensity inside the virial radius, in units of the critical density. We compute it using the fitting formula by Weinberg & Kamionkowski (2003) for $\Delta_{\rm vir} = \Delta_{\rm c}/\Omega_{\rm m}$, which is very similar to an earlier approximation by Nakamura (1996) given by Kitayama & Suto (1996) for a universe with arbitrary $\Omega_{\rm m}$.

A more general relation often used to fit observations makes use of a related normalization factor M_* and is given, at redshift $z = 0$, by

$$M_{200} \approx M_* \left(\frac{T}{4\ {\rm keV}}\right)^{\alpha}, \quad (6)$$

where M_{200} is the mass inside the sphere of mean overdensity 200 times higher than the critical density and $\alpha = 3/2$ in the hydrostatic equilibrium assumption (e.g. APP05). Hereafter, to account for redshift evolution, we normalize all our temperatures to $z = 0$ by dividing them by $E(z)^{2/3}$.

Measuring σ_8 from X-ray counts is affected by the degeneracy $\Omega_{\rm m}^{0.6}\sigma_8 \propto T_*^{-0.8}$ (Pierpaoli et al. 2003). Pierpaoli et al. (2003) have shown that the uncertainty in M_* is the main concern in measurements of σ_8 from X-ray cluster observations alone. Such data is

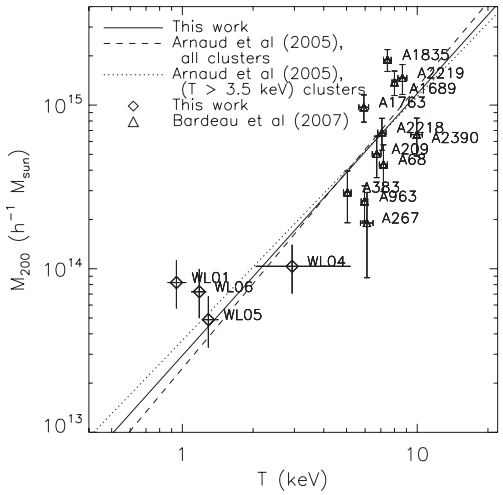

Figure 7. Mass–temperature relation, normalized to $z = 0$, for our group sample (diamonds). To improve the statistics, we added clusters from Bardeau et al. 2007 (triangles). We use X-ray temperature and weak lensing mass. The solid line is our best fit (equation 7). The dashed and dotted line are APP05 *M–T* relation, when they consider all clusters or only those with $T > 3.5$ keV, respectively.

limited by the requirement that the cluster masses be inferred from the X-ray profiles. Smith et al. (2003) have also shown that unrelaxed clusters, being hotter than relaxed clusters, provide a supplementary bias to the σ_8 estimate. It is thus important to have a mass estimate independent of the hydrostatic equilibrium assumption. Weak gravitational lensing gives such an estimate. Combined with X-ray temperature, it can be efficiently used to constraint the *M–T* relation, independently of the cluster physical state. Hjorth et al. (1998), Pedersen & Dahle (2006), Bardeau et al. (2007) have already used it to measure the *M–T* relation normalization.

As described above, we have the weak lensing mass and X-ray temperature of only four groups. Hence, to increase our statistics, we add the clusters of Bardeau et al. (2007) to our catalogue, providing us with 11 additional clusters. Bardeau et al. (2007) estimated cluster masses by fitting an NFW model to their tangential shears. We should note here that since the mass estimation of Bardeau et al. (2007) and ours are based on different techniques, our subsequent analysis of the *M–T* relation could be slightly biased due to possible calibration differences. Fig. 7 shows the relation between the temperature and the weak lensing mass M_{200} for the combined catalogues. Diamonds are our groups, labelled WL*id*, triangles are Bardeau et al. (2007) clusters, labelled A*id*. Bardeau et al. (2007) proceeded to the weak lensing analyses of massive haloes, the temperature of which were obtained by Zhang et al. (2007) and Ota & Mitsuda (2004); particularly, they estimated their weak lensing mass and measured the scale relations for those clusters. They fitted their sample by varying both α and M_*, and found a large slope, far from the hydrostatic equilibrium assumption, $\alpha = 4.6 \pm 0.7$. Doing the same analysis on the larger range in mass that the addition of both catalogues probes, from galaxy groups to galaxy clusters, we find

$$\frac{M_{200}}{10^{14}\,h^{-1}\,\mathrm{M}_\odot} = 2.71^{+0.79}_{-0.61}\left(\frac{T}{4\ \mathrm{keV}}\right)^{1.60\pm0.44}, \qquad (7)$$

which is in good agreement with APP05 (whether they use all clusters or only the most massive ones), Bardeau et al. (2007) (when they fix $\alpha = 1.5$), or Pedersen & Dahle (2006) or Hoekstra (2007). The solid line in Fig. 7 is our best fit. The dashed line is the best fit from APP05, when they consider all clusters in their catalogue. The dotted line is their best fit when they consider their most massive clusters ($T > 3.5$ keV).

Our result is consistent with self-similarity evolution for galaxy clusters down to low temperatures. It is also consistent with previous measurements which observe a steepening of the *M–T* relation at the low-mass end, due to the expected self-similarity breaking for such masses (e.g. Nevalainen et al. 2000; Finoguenov et al. 2001; APP05). Moreover, one must be aware that the galaxy groups we consider were detected just above our weak lensing selection function (Fig. 5). Due to the expected scatter in the *M–T* relation, those groups can represent only the most massive ones with temperature ranging about 1 keV. Our group sample could thus bias our fit towards a flat slope for the *M–T* relation. The analysis of more low temperature groups will be needed to further explore this issue.

5 DISCUSSION

The power-spectrum normalization σ_8 has been measured with different probes, such as X-ray clusters of galaxies, CMB, and cosmic shear (i.e. statistics of weak gravitational lensing). Some discrepancies have emerged between the preferred value from those measurements. Recent CMB observations favour a low σ_8 and cosmic shear used to emphasize a high value (see e.g. Refregier 2003a, for a review). X-ray clusters provide intermediate measurements (see e.g. Pierpaoli et al. 2003, for a review). The dominant discrepancy between cosmic shear and X-ray clusters has recently been reduced by Jarvis et al. (2006), who measured $\sigma_8 \approx 0.81$ for $\Omega_\mathrm{m} = 0.26$ when using cosmic shear alone, followed by Benjamin et al. (2007), who used the improved galaxy photometric redshifts of Ilbert et al. (2006), and measured $\sigma_8 = 0.84$ for $\Omega_\mathrm{m} = 0.24$ and Fu et al. (2008), who found a consistent value. To clarify these discrepancies, one needs to measure both the power-spectrum and the *M–T* relation normalizations σ_8 and M_*, as we discuss here.

The regions allowed for by different measurements on the T_*–$\sigma_8(\Omega_\mathrm{m}/0.24)^{0.6}$ plane are shown by Fig. 8. The shaded region shows the constraints given by our σ_8 and T_* measurements. Our best fits are shown by the thick lines. The slanted black band on the figure is the 68.3 per cent bound on the $\Omega_\mathrm{m}^{0.6}\ \sigma_8 \propto T_*^{-0.8}$ relation from Pierpaoli et al. (2003) using X-ray clusters. Its intersection with the vertical light blue band (APP05's T_* estimation) gives the current value for σ_8 favoured by X-ray cluster observations, $\sigma_8 \approx 0.77 \pm 0.06$ for an $\Omega_\mathrm{m} = 0.3$ universe (e.g. Pierpaoli et al. 2003), which corresponds to $\sigma_8(\Omega_\mathrm{m}/0.24)^{0.6} \approx 0.88 \pm 0.05$. This value is higher than that measured by Spergel et al. (2007) from CMB analyses of *WMAP*3 (dark blue), but lower than most cosmic shear analysis, like that of Hoekstra et al. (2006) made with CFHTLS wide data (red). This highlights the discrepancy between X-ray and weak lensing estimates of σ_8 mentioned above. However, Benjamin et al. (2007) give a lower estimate for σ_8, consistent with X-ray measurements (green). This could be a sign that other cosmic shear analyses did not take some systematics into account, and have thus overestimated σ_8. According to Benjamin et al. (2007), previously published analyses made use of insufficiently accurate galaxy photometric redshifts. Using the redshifts of Ilbert et al. (2006) yielded a lower value of σ_8 both for cosmic shear (Benjamin et al. 2007) and for our cluster count analysis. We found a 5 per cent decrease in our σ_8 estimation when going from previous redshift distributions to Ilbert et al. (2006) ones. This is less than the change reported by Benjamin et al. (2007), and our best fit still tends to favour a higher value for σ_8, but is limited by low statistics. Smith et al. (2003) have analysed the

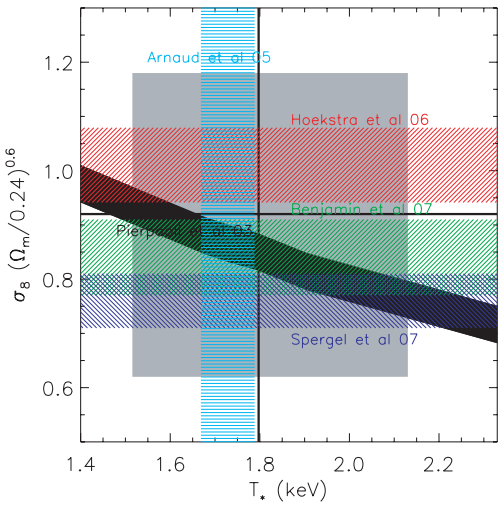

Figure 8. Domain allowed for by different measurements, in the T_*–σ_8 $(\Omega_m/0.24)^{0.6}$ plane. The shaded region shows the constraints given by our σ_8 and T_* measurements. Thick lines are our best fits. The slanted black region correspond to the 1 σ constraints on the $\Omega_m^{0.6}\sigma_8 \propto T_*^{-0.8}$ relation from Pierpaoli et al. (2003). The vertical, light blue, shaded region shows the 1σ error on T_* from APP05. CMB derived constraints of σ_8 (Spergel et al. 2007) are shown by the horizontal dark blue shaded region. Cosmic shear σ_8 estimations from Hoekstra et al. (2006) and Benjamin et al. (2007) are marked by the red and green horizontal shaded regions. The constraints of Hoekstra et al. (2006) are typical of cosmic shear results. They are higher than X-ray estimations, marked by the intersection between the allowed domains of Pierpaoli et al. 2003 and APP05.

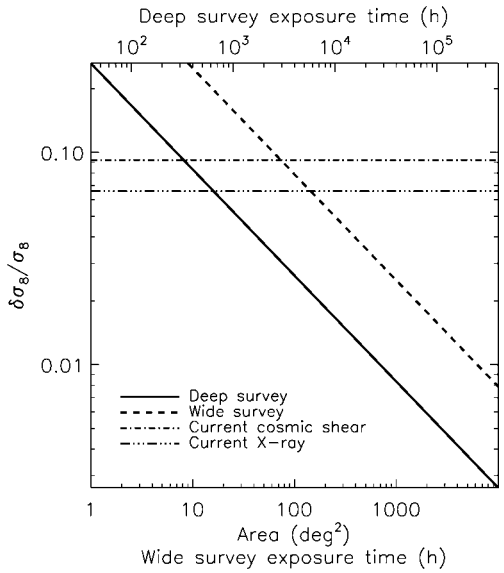

Figure 9. Relative errors on σ_8, from clusters counts in a weak gravitational lensing survey, as a function of survey size and integration time. All other parameters are kept constants. We assume that 1 deg^2 of wide requires 1 h of observation time, and 1 deg^2 of deep requires 40 h of observation time. That is, the lower x-axis shows area as well as the wide survey exposure time; the upper x-axis shows the deep survey exposure time. The thick solid line corresponds to a deep survey, and the thick dashed line to a wide survey. The flat lines show the current error measurement from cosmic shear statistics (dash–dotted, Hoekstra et al. 2006; Benjamin et al. 2007), and from X-ray clusters (dash–dot–dotted, Pierpaoli et al. 2003; APP05).

bias from unrelaxed clusters in σ_8 measurement using lensing clusters and the M–T relation. They found that unrelaxed clusters are 30 per cent hotter than relaxed clusters: using unrelaxed clusters can provide 20 per cent overestimates of σ_8. This is enough to explain the large range of measured σ_8, from $\approx$0.6 to $\approx$1. They estimated $\sigma_8(\Omega_m/0.24)^{0.6} = 0.86 \pm 0.23$. Estimates from X-ray alone can also be affected by systematics, such as the mass estimate from X-ray profiles of clusters. For example, a slight decrease of T_* would cause an increase of the X-ray estimate for σ_8. A better insight into this will come from an accurate measurement of T_*, preferably with mass estimation methods independent of cluster physics. Large combined weak lensing and X-ray surveys will be needed to disentangle the situation. They will provide both independent constraints on σ_8, and insights on T_*.

6 PROSPECTS FOR FUTURE SURVEYS

In the following, we investigate the impact of future combined blind weak lensing and X-ray surveys on the measurement precision of the power-spectrum and the M–T relation normalizations. We take the *WMAP*3 (Spergel et al. 2007) cosmology as our fiducial model. We consider two different ground-based survey strategies for our weak gravitational lensing analysis: deep and wide surveys similar to the CFHTLS Deep and Wide Surveys. We use their observed weighted number density of useful background galaxies to be $n_g =$ 20 arcmin^{-2} and 9 arcmin^{-2}, respectively, distributed according to equation (3). We also assume the intrinsic ellipticity and shape measurement error to be $\sigma_\gamma = 0.3$ in both cases. Following the CFHTLS scheduling, we take for exposure times 40 h deg^{-2} for the deep survey and 1 h deg^{-2} for the wide survey.

6.1 σ_8 measurements

We first investigate the impact of future surveys on the σ_8 measurement. Using the Press–Schechter approach described in Section 4.2.2, we estimate the number of weak lensing detections with significance higher than 2.5, taking into account shot noise and sample variance. We assume that all clusters have a spherically symmetrical NFW profile. We thus neglect the effect of haloes' asphericity shown by Clowe et al. (2004): triaxial haloes oriented along the line of sight appear more massive than triaxial haloes of the same mass, but perpendicular to the line of sight, and thus have a higher signal-to-noise ratio. Clowe et al. (2004) have shown that this approximation does not yield any difference in the mass measurement dispersion. Fig. 9 shows the 68.3 per cent relative error on σ_8 that can be reached by counting weak lensing detected clusters as a function of their significance, for a deep (thick solid line) and a wide (thick dashed line) surveys, as a function of survey's size and observing time. Because of the higher number density of clusters it allows one to detect, a deep survey provides errors three times lower than a wide survey of the same size. However, for a given exposure time, a wide survey provides errors 2.1 times lower than a deep one. That means that the gain due to the coverage (and detectable cluster number) increase is faster than the one due to depth increase. A larger coverage is also advantageous in that it makes sample variance fall down rapidly. Moreover, a wide survey detects the most massive haloes, the physics of which is better understood. Consequently, in a survey strategy driven by exposure time, one should prefer a wide survey. The flat dash–dotted line shows the current constraints provided by cosmic shear analyses (Hoekstra et al. 2006; Benjamin et al. 2007). The flat dash–dot–dotted line shows the current constraints from the

combination of X-ray M_* measurement (APP05) and X-ray cluster counts (Pierpaoli et al. 2003).

Detecting and counting clusters on a 10 deg^2 deep survey will be competitive with current cosmic shear measurements, whereas 20 deg^2 of coverage is needed to compete with current X-ray clusters measurements. Those figures transform as 100 and 200 deg^2 for a wide survey. That is, to compete with current cosmic shear surveys, one needs 400 h of deep survey exposure, or 100 h of wide survey exposure. Double these times are required to compete with X-ray surveys. A wide survey, less demanding in exposure time than a deep one, should then be used. Counting clusters on the entire planned CFHTLS Wide Survey 170 deg^2 will provide a 6 per cent fractional error on the σ_8 measurement. Reaching the 1 per cent fractional error will require a 7000 deg^2 wide survey, or a 700 deg^2 deep survey. Future surveys (e.g. Pan-STARRS,[3] LSST,[4] DUNE[5]) will be able to achieve such errors.

6.2 T_* measurements

We now turn to the precision that can be reached on T_* measurements by future joint surveys. What matters here is not cluster counts as a function of significance, but as a function of mass. As we see from Fig. 5, low-mass clusters of galaxies cannot be seen through weak gravitational lensing since they do not create high enough signal-to-noise ratios. A deep survey captures lower mass clusters than a wide survey, but deep and wide surveys give access to the same number of massive clusters. Therefore, a deep survey is naturally focused on the physics of galaxy groups (e.g. it can probe similarity breaking at the low-mass end of the M–T relation). A wide survey gives the same statistics on massive haloes, generally used to measure the M–T relation normalization: for this purpose, one should then choose a wide survey. To compare the merits of both deep and wide survey on the T_* estimation's precision, we simulate M–T relations for both types of survey. We take a realistic scatter into account, $\sigma_{\log,\mathrm{int}} = 0.051$ for the logarithmic M–T relation (APP05). We assume that masses are measured through weak gravitational lensing. We measure T_* and the error on its estimate, by assuming (1) that our cluster sample is complete, (2) that we only make use of those clusters detected in our blind survey and (3) that we know the X-ray temperature of each of them. We also investigate the influence of the mass estimation fractional error $\delta M/M$.

Fig. 10 shows the 68.3 per cent error on T_* that can be reached from a combined blind X-ray and deep (solid lines) or wide (dashed lines) weak gravitational lensing surveys, as a function of survey's size and integration time. Here again, as for the error on the power-spectrum normalization, a deep survey gives errors 2.3 times lower than a wide one with the same sky area coverage. On the other hand, a wide survey gives errors 2.7 times lower than a deep one with the same exposure time. The dependence on area underlines the reliance of T_* estimation on the number of useable haloes for the M–T relation fitting. Fig. 10 also shows the sensitivity of the T_* estimation to the mass measurement errors. The black lines assume $\delta M/M = 0.2$, and the red ones $\delta M/M = 0.3$, which are the current fractional errors on mass measurement from weak lensing. Going from $\delta M/M = 0.3$ to 0.2 allows one to reduce the error on T_* by a factor of 1.3 (respectively 1.2) for a deep (respectively wide) survey of a given sky area. The flat solid line represents the current error

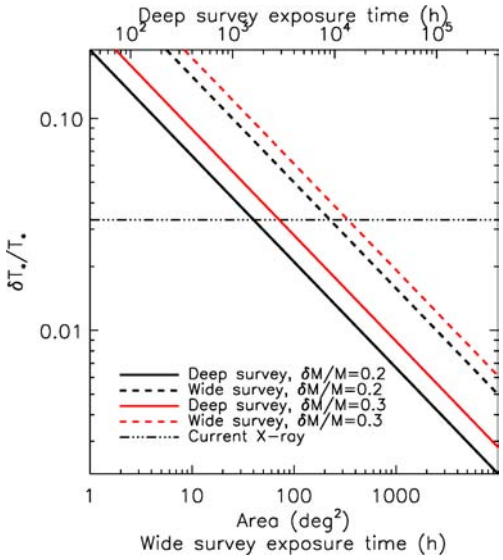

Figure 10. Relative errors on T_* from combined weak gravitational lensing and X-ray surveys, as a function of survey size and integration time. All other parameters are kept constants. The lower x-axis shows area as well as the wide survey exposure time; the upper x-axis shows the deep survey exposure time. Solid lines show the errors for a deep survey, assuming the fractional error on weak lensing mass measurement is 20 per cent (thick black) and 30 per cent (red). Dashed lines, with the same colour indexing, show the errors for a wide survey. The current error measurement from X-ray clusters is shown by the flat dash–dot–dotted line (Pierpaoli et al. 2003; APP05). We made the same assumption about the relation between survey area and observation time as in Fig. 9.

on T_* from X-ray clusters (APP05). Assuming a 20 per cent error measurement on weak lensing masses, one needs a 50 (respectively 300) deg^2 weak lensing deep (respectively wide) survey to reach the current error. Reaching the 1 per cent fractional error (for our fiducial model with $T_* = 1.9$) will require a 2500 deg^2 wide survey, or a 500 deg^2 deep survey. Weak lensing surveys like LSST or DUNE combined with X-ray surveys like eROSITA will be able to reach such a limit.

In a survey strategy driven by exposure time, a wide survey of 2500 deg^2 (2500 h) will be able to reach the 1 per cent accuracy both on σ_8 and T_*, at a much cheaper expense than a deep survey. Nevertheless, a deep survey will still be useful to probe high-redshift regions ($z \geqslant 0.8$), and to study low-mass clusters of galaxies ($M \leqslant 10^{14}\,h^{-1}\,\mathrm{M}_\odot$).

7 CONCLUSION

We have presented the first shapelet analysis of weak gravitational lensing surveys. We have constructed convergence maps of the CFHTLS Deep D1 field, and of 4 deg^2 of the CFTHLS Wide W1 field, which include the D1 field. We have detected six clusters of galaxies, through the lensing signal they generate. Our D1 map is in good agreement with that of GS07, precedentedly created using the KSB shear measurement method. We combined our weak lensing data with the X-ray analysis of *XMM*-LSS C1 clusters lying in the same region of the sky (Pacaud et al. 2007). These three clusters catalogue are consistent. All our shapelet detections have either an X-ray counterpart or a KSB detection. Counting our detections and accounting for the weak lensing selection function allowed us to constrain the power-spectrum normalization $\sigma_8(\Omega_\mathrm{m}/0.24)^{0.6} = 0.92^{+0.26}_{-0.30}$. The combination of lensing masses and X-ray temper-

[3] http://panstarrs.ifa.hawaii.edu.
[4] http://www.lsst.org.
[5] http://www.dune-mission.net.

atures provided us with a new measurement of the M–T relation normalization T_* (or equivalently M_*) for clusters of galaxies, $M_* = 2.71^{+0.79}_{-0.61} \times 10^{14}\, h^{-1}\, \mathrm{M}_\odot$. Our results, though limited by low statistics and sample variance, are consistent with other current estimates. We also measured the slope of the M–T relation, and found it consistent with self-similarity for low-mass clusters, $\alpha = 1.60 \pm 0.44$. We have shown that one must measure both σ_8 and T_* from combined weak lensing and X-ray surveys to investigate the discrepancy between independent measurements of σ_8 from different probes.

Weak lensing surveys are becoming more and more effective, and are currently being optimized for best extracting cosmological information. Optimal surveys will allow us to provide more accurate estimates of σ_8 and T_*, and to disentangle the current σ_8 issue (Amara & Refregier 2007). We have compared the merits of weak lensing deep and wide blind surveys, based on the CFHTLS, at estimating σ_8. We also looked at their merits at estimating T_* while combined with an X-ray survey on their region of the sky. We found that for experiments driven by exposure time constraints, a wide survey will give approximately three times lower errors on the estimates of both σ_8 and T_*. To secure the measurement of σ_8 and M_* with the current statistical accuracy, a 200- and a 300-deg^2 wide surveys will be needed, respectively. We finally found that a 7000-deg^2 wide survey will be able to reach the 1 per cent accuracy both on the power-spectrum and M–T relation normalizations.

ACKNOWLEDGMENTS

The authors wish to thank Hervé Aussel, Krys Libbrecht, Jean-Baptiste Melin, Yannick Mellier, Sandrine Pires, Trevor Ponman, Jean-Luc Starck, Geneviève Soucail and Romain Teyssier for useful discussions, and Cathy Horellou for comments on the first version of the paper.

REFERENCES

Amara A., Refregier A., 2007, MNRAS, 381, 1018
Arnaud M., Aghanim N., Neumann D. M., 2002, A&A, 389, 1
Arnaud M., Pointecouteau E., Pratt G. W., 2005, A&A, 441, 893 (APP05)
Bacon D., Refregier A., Ellis R., 2000, MNRAS, 318, 625
Bacon D., Massey R., Refregier A., Ellis R., 2003, MNRAS, 344, 673
Bardeau S., Soucail G., Kneib J. P., Czoske O., Ebeling H., Hudelot P., Smail I., Smith G. P., 2007, A&A, 470, 449
Bartelmann M., Schneider P., 2001, Phys. Rep., 340, 291
Basilakos S., 2003, ApJ, 590, 636
Basilakos S., Voglis N., 2007, MNRAS, 374, 269
Benjamin J. et al., 2007, MNRAS, 381, 702
Bertin E., Arnouts S., 1996, A&AS, 117, 393
Bialek J. J., Evrard A. E., Mohr J. J., 2001, ApJ, 555, 597
Boulade O. et al., 2003, in Masanori I., Moorwood A. F. M., eds, Proc. SPIE Vol. 4841, Instrument Design and Performance for Optical/Infrared Ground-based Telescopes. SPIE, Bellingham, p. 72
Castillo-Morales A., Schindler S., 2003, A&A, 403, 433
Chiappetti L. et al., 2005, A&A, 439, 413
Clowe D., De Lucia G., King L., MNRAS, 350, 1038
de Putter R., White M., 2005, New Astron., 10, 676
Eke C. R., Navarro J. F., Frenck C. S., 1998, ApJ, 503, 569
Ettori S., De Grandi S., Molendi S., 2002, A&A, 391, 841
Fahlman G., Kaiser N., Squires G., Woods D., 1994, ApJ, 437, 56
Finoguenov A., Reiprich T. H., Böhringer H., 2001, A&A, 368, 749
Fu L. et al., 2008, A&A, 479, 9
Gavazzi R., Soucail G., 2007, A&A, 462, 459 (GS07)
Hamana T., Takada M., Yoshida N., 2004, MNRAS, 350, 893
Heymans C. et al., 2005, MNRAS, 361, 160
Hjorth J., Oukbir J., van Kampen E., 1998, MNRAS, 298, L1
Hoekstra H., 2001, A&A, 370, 743
Hoekstra H., 2003, MNRAS, 339, 1155
Hoekstra H., 2007, MNRAS, 379, 317
Hoekstra H. et al., 2006, ApJ, 647, 116
Horellou C., Berge J., 2005, MNRAS, 360, 1393
Hu W., Kravtsov A. V., 2003, ApJ, 584, 702
Huterer D., White M., 2002, ApJ, 578, L95
Ilbert O. et al., 2006, A&A, 457, 841
Jarvis M., Jain B., Bernstein G., Dolney D., 2006, ApJ, 644, 71
Jenkins A., Frenck C. S., White S. D. M., Colberg J. M., Cole S., Evrard A. E., Couchman H. M. P., Yoshida N., 2001, MNRAS, 321, 372
Kaiser N., Squires G., 1993, ApJ, 404, 441
Kaiser N., Squires G., Broadhurst T., 1995, ApJ, 449, 460
Kitayama T., Suto Y., 1996, ApJ, 469, 480
Kneib J.-P., Mellier Y., Pello R., Miralda-Escude J., Le Borgne J.-F., Boehringer H., Picat J.-P., 1995, A&A, 303, 27
Kneib J.-P., Ellis R. S., Smail I., Couch W. J., Sharples R. M., 1996, ApJ, 471, 643
Lacey C., Cole S., 1993, MNRAS, 262, 627
Lokas E. L., 2001, Acta Phys. Pol. B, 32, 3643
Lokas E. W., Bode P., Hoffman Y., 2004, MNRAS, 349, 595
Luppino G. A., Gioia I. M., Hammer F., Le Fèvre O., Annis J. A., 1999, A&A, 136, 117
Manera M., Mota D. F., 2006, MNRAS, 371, 1373
Maor I., Lahav O., 2005, JCAP, 07, 003
Marian L., Bernstein G., 2006, Phys. Rev. D, 73, 123525
Massey R., Refregier A., 2005, MNRAS, 363, 197
Massey R., Refregier A., Bacon D., Ellis R., Brown M. L., 2005, MNRAS, 359, 1277
Massey R. et al., 2007a, ApJS, 172, 230
Massey R. et al., 2007b, Nat, 445, 286
Massey R. et al., 2007c, MNRAS, 376, 13
Massey R., Rowe B., Réfrégier A., Bacon D., Bergé J., 2007d, MNRAS, 380, 229
Mellier Y., 1999, ARA&A, 37, 127
Mellier Y., Fort B., Kneib J.-P., 1993, ApJ, 407, 33
Metzler C. A., White M., Loken C., 2001, ApJ, 547, 560
Miyazaki S. et al., 2002, ApJ, 580, L97
Miyazaki S., Hamana T., Ellis R. S., Kashikawa N., Massey R. J., Taylor J., Refregier A., 2007, ApJ, 669, 714
Muanwong O., Thomas P. A., Kay S. T., Pearce F. R., 2002, MNRAS, 336, 527
Munshi D., Valageas P., van Waerbeke L., Heavens A., 2006, preprint (astro-ph/0612667)
Nakamura T. T., 1996, Master's thesis, Univ. Tokyo
Nevalainen J., Markevitch M., Forman W., 2000, ApJ, 532, 694
Nunes N. J., da Silva A. C., Aghanim N., 2006, A&A, 450, 899
Ota N., Mitsuda K., 2004, A&A, 428, 757
Pacaud F. et al., 2006, MNRAS, 372, 578
Pacaud F. et al., 2007, MNRAS, 382, 1289
Padmanabhan T., 1993, Structure Formation in the Universe. Cambridge Univ. Press, Cambridge
Paulin-Henriksson S., Antonuccio-Delogu V., Haines C. P., Radovich M., Mercurio A., Becciani U., 2007, A&A, 467, 427
Pedersen K., Dahle H., 2007, ApJ, 667, 26
Peebles P. J. E., 1980, The Large-Scale Structure of the Universe. Princeton Univ. Press, Princeton, NJ
Pierpaoli E., Borgani S., Scott D., White M., 2003, MNRAS, 342, 163
Pierre M. et al., 2004, JCAP, 9, 11
Pierre M. et al., 2006, MNRAS, 372, 591
Press W. H., Schechter P., 1974, ApJ, 187, 425
Rasia E. et al., 2006, MNRAS, 369, 2013
Reblinsky K., Bartelmann M., 1999, A&A, 345, 1
Refregier A., 2003a, ARA&A, 41, 645
Refregier A., 2003b, MNRAS, 338, 35
Refregier A., Bacon D., 2003, MNRAS, 338, 48
Rhodes J., Refregier A., Groth E. J., 2001, ApJ, 552, L85

Schrabback T. et al., 2007, A&A, 468, 823
Seljak U., 2002, MNRAS, 337, 769
Semboloni E. et al., 2006, A&A, 452, 51
Smail I., Ellis R. S., Dressler A., Couch W. J., Oemler A. J., Sharples R. M., Butcher H., 1997, ApJ, 479, 70
Smith G. P., Edge A. C., Eke V. R., Nichol R. C., Smail I., Kneib J.-P., 2003, ApJ, 570, L79
Smith G. P., Kneib J.-P., Smail I., Mazzotta P., Ebeling H., Czoske O., 2005, MNRAS, 359, 417
Spergel D. N. et al., 2007, ApJS, 170, 377
Starck J. L., Murtagh F., Bijaoui A., 1998, Image Processing and Data Analysis: The Multiscale Approach. Cambridge Univ. Press, Cambridge
van Waerbeke L. et al., 2000, A&A, 358, 30
van Waerbeke L., White M., Hoekstra H., Heymans C., 2006, Astropart. Phys., 26, 91
Viana P. T. P., Liddle A. R., 1996, MNRAS, 281, 323
Vikhlinin A., Kravtsov A., Forman W., Jones C., Markevitch M., Murray S. S., Van Speybroeck L., 2006, ApJ, 640, 691
Wang L., Steinhardt P. J., 1998, ApJ, 508, 483
Weinberg N. N., Kamionkowski M., 2003, MNRAS, 341, 251
Willis J. P. et al., 2005, MNRAS, 363, 675
Wittman D. M., Tyson J. A., Kirkman D., Dell'Antonio I., Bernstein G., 2000, Nat, 405, 143
Wittman D. M., Dell'Antonio I. P., Hughes J. P., Margoniner V. E., Tyson J. A., Cohen J. G., Norman D., 2006, ApJ, 643, 128
Zhang Y. Y., Finoguenov A., Böhringer H., Kneib J. P., Smith G. P., Czoske O., Soucail G., 2007, A&A, 467, 437

This paper has been typeset from a TEX/LATEX file prepared by the author.